Measurement 199 (2022) 111569

Contents lists available at ScienceDirect

Measurement

journal homepage: www.elsevier.com/locate/measurement

Geometrical deviation modeling and monitoring of 3D surface based on multi-output Gaussian process

Chen Zhao [a], Jun Lv [b], Shichang Du [a,*]

[a] Department of Industrial Engineering and Management, School of Mechanical Engineering, Shanghai Jiao Tong University, Shanghai, China
[b] Faculty of Economics and Management, East China Normal University, Shanghai, China

ARTICLE INFO

Keywords:
Three-dimensional surface
Geometrical deviation
Spherical mapping
Multi-output Gaussian process

ABSTRACT

Geometrical deviation is an important factor in determining the quality of a three-dimensional (3D) Surface. For 3D surfaces with complex shapes, the high-definition measurement (HDM) technology can provide detailed information on surface topography, which inspired new challenges in characterizing, modeling, and monitoring geometrical deviations. This paper proposes a spherical multi-output Gaussian process (S-MOGP) method to model and monitor 3D surfaces. Firstly, the surface in the 3D coordinate system is mapped to the spherical 2D parameter domain. Secondly, a state equation based on the multi-output Gaussian process is established to model the 3D surface. Finally, statistics are calculated and control charts are presented to monitor the geometrical deviation. The results of simulations and a case study show that the proposed method can effectively model 3D surfaces and monitor the geometrical deviations.

1. Introduction

Geometrical deviation, which refers to the variation of a measured element relative to its ideal element, is an important factor affecting the quality and accuracy of parts, such as straightness, flatness, circularity and cylindricity. With the improvement of processing and measurement technology, the processing quality of three-dimensional (3D) surfaces has become an important research topic. Geometrical deviations are important control objects of 3D surfaces and particularly impact the sealing, reliability, and life of products [1,2].

To evaluate the processing quality of 3D surfaces, measurement data must first be obtained. Currently, the commonly used method is the section curve method based on three-coordinate surface measurements [3]. However, this method has low measurement efficiency and the limited section curve cannot fully characterize the processing quality of the entire surface, resulting in the missed detection of local areas. With the advancement of non-contact measurement technology, high-definition measurement (HDM) technology can collect millions of data points that can entirely reflect the geometry information of manufactured surfaces. Therefore, inferring, reconstructing, and monitoring 3D surfaces from large-scale point cloud measurements has become novel research.

In many applications, assessing the quality of a process or product is characterized by a functional relationship between response and explanatory variables. The stability of these relationships over time is monitored and viewed through statistical process control (SPC). Woodall [4] summarized these methods as profile monitoring. Early profile monitoring research began with a simple linear regression model. To represent more complicated shapes, Kazemzadeh et al. [5] and Zou et al. [6] proposed polynomial and multiple regression models. Colosimo et al. [7] explored a spatial autoregressive regression (SARX) model to study circular profiles. Zhao et al. [8] extend the model to a cylindrical surface. These monitoring efforts can be extended to the quality of multiple surface characteristics, such as roundness, flatness, and cylindricity.

Most profile monitoring research has been focused on the case where the profile is two-dimensional (2D) and can be represented by a regression model. Wells et al. [9] suggested that monitoring efforts can be extended to 3D space with the aid of point cloud datasets. However, due to the arbitrariness of 3D surfaces, profiles cannot simply be represented by a specific equation. Therefore, compared with evaluation methods for 3D surface textures, the research on the geometrical deviation of 3D surfaces is limited [10].

The existing modeling and monitoring methods for 3D surfaces can be divided into three types: deviation method, feature extraction method, and parametric surface method, as shown in Fig. 1.

* Corresponding author.
E-mail addresses: zhao_chen@sjtu.edu.cn (C. Zhao), jlv@dbm.ecnu.edu.cn (J. Lv), lovbin@sjtu.edu.cn (S. Du).

https://doi.org/10.1016/j.measurement.2022.111569
Received 19 December 2021; Received in revised form 12 March 2022; Accepted 26 June 2022
Available online 6 July 2022

(i) Deviation method. This method evaluates the 3D surface error by calculating the deviation between the measured value and the nominal surface. To evaluate the deviation, it is necessary to convert the measured surface to an accurate position relative to the design surface for surface matching. This process usually uses the least square method or the minimum area method to obtain the rigid body conversion matrix required for matching [11]. Zang and Qiu [12,13] calculated the translation and rotation matrix of the measured value relative to the nominal point cloud to monitor the surface quality of 3D printing. This method can be applied to 3D surface with regular and sparse measurement points. Stankus and Castillo-Villar [14] divided the point cloud into regions of interest (ROIs) and calculated the mean deviation for each ROI. Mehrad et al. [15] and Wells et al. [9] used B-spline to reconstruct the 3D surface, and the geometric deviations of the surface are reflected by the position of the spline control points. Deviation methods need to achieve the best matching state between the measurements and the theoretical surface. The deviation from the measurements to the ideal surface depends on the registration accuracy. This calculation is applicable to a known CAD model surface or a series of theoretical data points.

(ii) Feature extraction method. In some cases, the quality of surface can be described by relevant macro or micro-geometrical descriptors, such as length, high, roughness, and normal vector [16]. However, these features are highly sensitive to local defects and cannot qualitatively and quantitatively represent the contour change of the measurement surface relative to the theoretical surface. In response to this problem, Kase et al. [17] proposed a local and global evaluation method for the geometric deviation of 3D surface. The local evaluation method calculates the principal curvature change between a CAD model and an actual surface. The overall evaluation method uses aggregate normal vectors to characterize various parts of the surface. Wang and Tsung [18] and Wells et al. [19] used the quantile–quantile (Q-Q) plot method to monitor 3D surfaces. The Q-Q plot converts high-dimensional data into a series of linear profiles to determine whether two sets of data come from the same distribution. Osada et al. [20] and Laga et al. [21] used distribution histograms to represent the shape characteristics of 3D surfaces. However, by converting point clouds into distribution maps, the information about local changes in the complex-shaped 3D surface will be lost. Huang et al. [22] divided a 3D surface into a series of plane sub-regions by surface segmentation and evaluated the surface quality by extracting the normal vector and wavelet packet entropy of the sub-regions. Taken overall, the feature extraction method cannot specifically reflect the surface shape, so it is difficult to fully characterize the geometric deviation.

(iii) Parametric surface method. This method establishes a regression model to model the shape of 3D surface. Colosimo et al. [23] modeled a cylindrical surface through Gaussian process (GP) and monitored the surface quality by the deviation value of checkpoints. Zhao et al. [24] used the height value as the response value of the abscissa and ordinate for the 3D surface and used Gaussian process regression (GPR) to model the 3D surface. Parametric surface method establishes a regression model for each measuring surface and the geometrical deviation of 3D surface can be monitored through model parameters. The advantage of surface parameterization is that it avoids the precise registration of surfaces, fully reflects the information of the surface shape, and can provide a valuable reconstruction method for reverse engineering. Most current parametric methods regard surface data as a special profile with one response variable and two explanatory variables. However, this assumption is limited and does not conform to the three degrees of freedom in the actual measurements.

To overcome the limitations of parametric models, Castillo et al. [25] used manifold learning to map 3D surfaces into 2D space, and proposed a Geodesic Gaussian process (GGP) method to model the relationship between the mapped surfaces and the actual surfaces. This method reconstructs a underlying surface via 2D manifold learning, which can reflect the distance correlation between two points on the surface more realistically. A similar approach is the Gaussian process latent variable model (GPLVM) proposed by Lawrence [26]. GPLVM introduced an additional set of latent variables and described the descriptive information through a nonlinear dimension reduction model. The key idea of these approaches are that high-dimensional data may really lie on the low-dimensional nonlinear manifold that one wishes to model [27].

Existing dimensionality reduction methods are dedicated to reducing high-dimensional data to low-dimensional space. For the 3D surface, commonly used dimension reduction methods such as GPLVM, Locally Linear Embedding (LLE), isometric mapping, etc. are all plane parameterization methods, and the main defect is that they cannot be directly implemented on closed surface models.

For manufacturing surfaces, geometric models are often described by closed, genus-0 surfaces, i.e., deformed spheres. For such models, the sphere is the most natural parametrization domain. Therefore, for the closed surfaces, the sphere can be regarded as the underlying surface and the spherical mapping is considered to reduce the dimension of three-dimensional surface, so that the points on the low-dimensional space have a reasonable and uniform structure, and an effective mapping result can be formed for closed surfaces.

Furthermore, according to Sun et al. [28], the data obtained from the machined surface by non-contact measurement is Gaussian distribution and has a strong spatial correlation. Considering this spatial correlation, the relationship between latent spatial data and the real surface can be modeled by Gaussian process.

The aim of this study is to explore a regression model that can be applied to closed surfaces. Based on spherical mapping and multi-output Gaussian process (MOGP), a spherical multi-output Gaussian process (S-MOGP) method is proposed to model the 3D surface. Meanwhile, considering the large-scale structure of point cloud, the compactly supported covariance matrix function is constructed to reduce computational complexity. Moreover, the geometrical deviation is monitored by the deviation between the measured surface and the predicted value.

The advantage of the proposed method is that: (i) the model of 3D

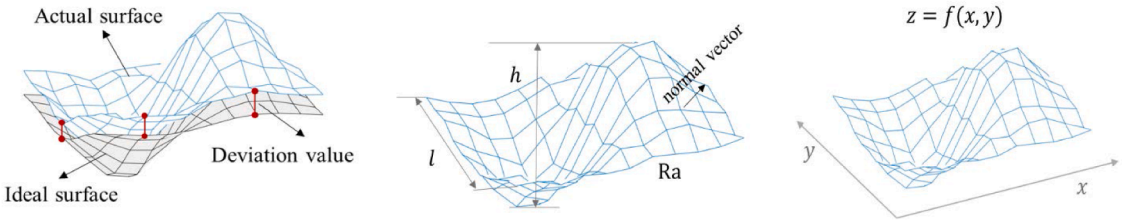

(a) Deviation method (b) Feature extraction method (c) Parametric surface method

Fig. 1. Schematic diagram of geometric deviations evaluation of three methods.

surface is established through spherical mapping, and the angle distance is used instead of Euclidean distance and Geodesic distance, which is suitable for closed and non-expandable surfaces. (ii) A regression model is established based on MOGP to fit the 3D surface shape and the x, y, and z directions are comprehensively modeled, considering the spatial correlation of measurement points. (iii) This method can be used for modeling and monitoring point clouds with large-scale datasets.

The remaining part of this work is organized as follows. Section 2 reviews related prior work on surface parameterization and MOGP. Section 3 describes the proposed method. A simulation and a real case study are shown in Section 4 and Section 5, respectively. Section 6 concludes the paper.

2. Related prior work

2.1. Spherical mapping

Surface parameterization creates a one-to-one mapping from a surface to a certain parameter domain, i.e., mapping from one surface to another. The parameter surface is defined by a vector-valued parameterized function ϕ: $\Omega \rightarrow S$, which maps the surface $\Omega \subset \mathbb{R}^3$ to the 2D parameter domain $S \subset \mathbb{R}^2$.

Mapping from a surface to the parameter domain requires minimizing certain types of distortion. The length distortion, angle distortion and area distortion are the most common type of distortions, corresponding to Isometric map, Conformal map and Equiareal map methods. In practice, surface parameterization considers the topology of the generated data, aims to minimize a certain type of distortion or a combination of different distortions [29].

A 3D geometric model can usually be represented by a deformed sphere; therefore, a sphere is the most natural parameterized domain of 3D surfaces [31]. Given a surface M, the spherical mapping is specified by assigning each vertex a parametrization to form a continuous reversible mapping from the surface to the sphere ϕ: M → S. The parametric method of the spherical surface is invariant to translation, rotation, and scaling, and it is suitable for describing point clouds [32].

The point cloud data obtained by the measurement is stored in the Cartesian coordinate system of 3D space. Each point is represented by three coordinate values (x, y, z). When the measurement coordinate system is inconsistent, the measured object should be aligned by rotation and translation (refer to the PCA-based coarse registration used by Yao et al. [33]). In the spherical coordinate system, each point is represented by a pair of radian values (u, v), where elevation $u \in [-\pi/2, \pi/2]$ and azimuth $v \in [-\pi, \pi]$. The spherical coordinate of (x, y, z) is

$$r(u, v) = (\mathrm{R}\cos u \cos v,\ \mathrm{R}\cos u \sin v,\ \mathrm{R}\sin u) \tag{1}$$

Therefore, the value of (x, y, z) in a 3D surface can be represented by two parameters (u, v).

For spherical surfaces, first, perform spherical fitting to find the approximate center of the sphere, and then move the center of the sphere to the origin of the coordinate system. Fig. 2 is a schematic diagram of spherical mapping.

For the spherical parameterization of complex surfaces, many scholars have proposed different methods to parameterize the 3D surface onto the sphere. This paper focuses on the one-to-one correspondence between the points on the original surface and the sphere parameter domain, rather than equal area or equal arc length mapping. Therefore, the conformal method is used to parameterize the surface of the sphere.

Based on the conformal parameterization method, Shen et al. [29] and Choi et al. [34] performed the spherical mapping by solving a series of Laplace equations. The specific steps of spherical parameterization are given in Appendix A.

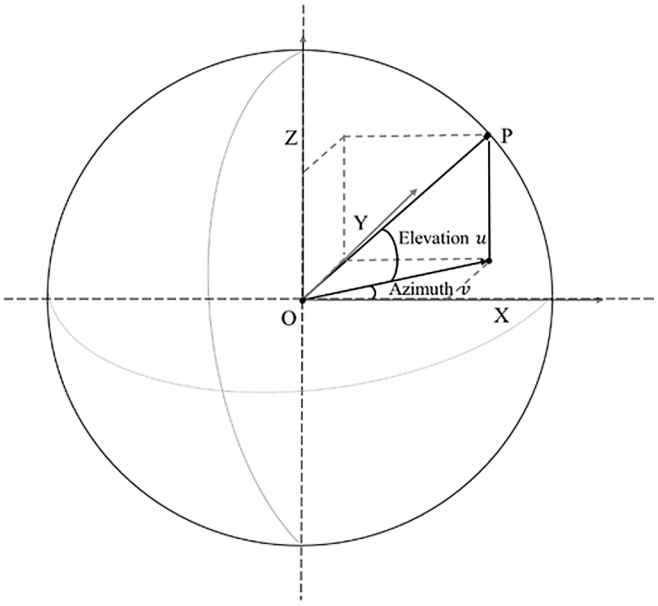

Fig. 2. Spherical domain.

2.2. Gaussian process regression

GP is a random process composed of an infinite number of random variables that obey the Gaussian distribution defined in a continuous domain. GPR is a non-parametric model that uses GP priori to perform regression analysis on data. In function-space view, the idea of GPR is to find a function set from countless functions which meets the test data. According to the prior information, the distribution of the function set is calculated through the properties of Bayesian rule and Gaussian distribution. The distribution of the set is used to predict the subsequent data.

Given a paired dataset of N observations: $D = \{(x_n, y_n) | n = 1, \cdots, N\}$, $\mathbf{x}$ and $\mathbf{y}$ are input and output vectors. In GPR, $\boldsymbol{y} = f(\boldsymbol{x}) + \boldsymbol{\varepsilon}$, $\boldsymbol{\varepsilon}\ N(0, {\sigma_n}^2)$, where ${\sigma_n}^2$ is the noise variance. $f(\boldsymbol{x})$ is the latent function which implies that any finite subset of latent variables has a multivariate Gaussian distribution, denoted by

$$f(\boldsymbol{x}) \sim GP(m(\boldsymbol{x}), k(\boldsymbol{x}, \boldsymbol{x}')) \tag{2}$$

where $m(\boldsymbol{x})$ is mean function, which is usually taken as zero without loss of generality. $k(\boldsymbol{x}, \boldsymbol{x}')$ is the covariance function.

In training observations $\{x_i, y_i\}_{i=1}^n$, the input data is $\boldsymbol{x} = \{x_1, \cdots, x_n\}^{\mathrm{T}} \in \mathbb{R}^{1 \times n}$, and the output data is $\boldsymbol{y}$. The joint prior distribution of the test points $\boldsymbol{x}_*$ and the predictive targets $\boldsymbol{f}_*$ is

$$\begin{bmatrix} \boldsymbol{y} \\ \boldsymbol{f}_* \end{bmatrix} \sim N\left(0, \begin{bmatrix} K(X, X) + \sigma_n^2 I & K(X, X_*) \\ K(X_*, X) & K(X_*, X_*) \end{bmatrix}\right) \tag{3}$$

where K(X, X) is the covariance matrix with the element $\mathrm{K}_{ij} = k(x_i, x_j)$. X_* is the matrix of test inputs, and X is the matrix of the training inputs.

Each element of the covariance matrix is the correlation measure of the corresponding two x values. Covariance matrix is the symmetric and positive semi-definite (PSD) matrix and can be calculated by the kernel function.

After observing the training sample, the posterior distribution of the test output function is

$$\boldsymbol{f}_* | X, \boldsymbol{y}, X_* \sim N(\bar{\boldsymbol{f}}_*, \mathrm{cov}(\boldsymbol{f}_*)) \tag{4}$$

where

$$\bar{\boldsymbol{f}}_* = \mathrm{K}(\mathrm{X}_*, \mathrm{X})\left[\mathrm{K}(\mathrm{X}, \mathrm{X}) + {\sigma_n}^2 I\right]^{-1} \boldsymbol{y} \tag{5}$$

$$\mathrm{cov}(\boldsymbol{f}_*) = \mathrm{K}(\mathrm{X}_*,\mathrm{X}_*) - \mathrm{K}(\mathrm{X}_*,\mathrm{X})\left[\mathrm{K}(\mathrm{X},\mathrm{X}) + {\sigma_n}^2 I\right]^{-1}\mathrm{K}(\mathrm{X},\mathrm{X}_*) \tag{6}$$

For multivariate GP, the above methods are still valid. The difference is that the kernel function in the multivariate GP represents the correlation of the two vectors.

The key to the GP model is the covariance function (kernel function), which directly determines the covariance between the function values. The GP corresponding to different covariance functions have different regression effects, but they all need to satisfy the semi-definite form. Commonly used kernel functions include Gaussian kernel function, Matern kernel, square exponential kernel function, periodic kernel function, etc.

2.3. Multi-output Gaussian process regression

For multi-output tasks, ordinary GPR can only model each output separately and cannot consider the correlation between the outputs. Some scholars consider using the correlation between outputs to establish a multi-output Gaussian process (MOGP) model to improve the prediction accuracy [30]. Here is a brief introduction to MOGP.

For training points $X = \{x_1, \cdots, x_n\}^{\mathrm{T}}$, there are D-dimensional output $\mathrm{Y} = (y_1, \cdots, y_D)^{\mathrm{T}}$. Function $f(\boldsymbol{x})$ are assumed to follow GP as $f(\boldsymbol{x})$ $GP(0, \mathrm{K}(\boldsymbol{x},\boldsymbol{x}^{'}))$, and the covariance function is

$$\mathrm{K}(\boldsymbol{x},\boldsymbol{x}^{'}) = \begin{bmatrix} k_{11}(\boldsymbol{x},\boldsymbol{x}^{'}) \cdots k_{1\mathrm{D}}(\boldsymbol{x},\boldsymbol{x}^{'}) \\ \vdots \ddots \vdots \\ k_{\mathrm{D}1}(\boldsymbol{x},\boldsymbol{x}^{'}) \cdots k_{\mathrm{DD}}(\boldsymbol{x},\boldsymbol{x}^{'}) \end{bmatrix} \in \mathbb{R}^{D\times D} \tag{7}$$

The joint distribution of multiple outputs can be written as

$$\begin{bmatrix} Y \\ f_* \end{bmatrix} \sim MN\left(0, \begin{bmatrix} K(X,X) + \sigma_n^2 I & K(X,X_*) \\ K(X_*,X) & K(X_*,X_*) \end{bmatrix}\right) \tag{8}$$

where $K(X,X) \in \mathbb{R}^{nD\times nD}$ is the covariance matrix.

Given the training set X and the output observations Y, the posterior distribution of the tested output function is: $\boldsymbol{f}_*|\mathrm{X},\mathrm{Y},\mathbf{x}_* \sim \mathrm{N}(\bar{\boldsymbol{f}}_*, \mathrm{cov}(\boldsymbol{f}_*))$. The prediction mean and prediction variance are given as

$$\bar{\boldsymbol{f}}_* = K(X_*,X)\left[K(X,X) + \sigma_n^2 I\right]^{-1} Y \tag{9}$$

$$\mathrm{cov}(\boldsymbol{f}_*) = K(X_*,X_*) - K(X_*,X)\left[K(X,X) + \sigma_n^2 I\right]^{-1} K(X,X_*) \tag{10}$$

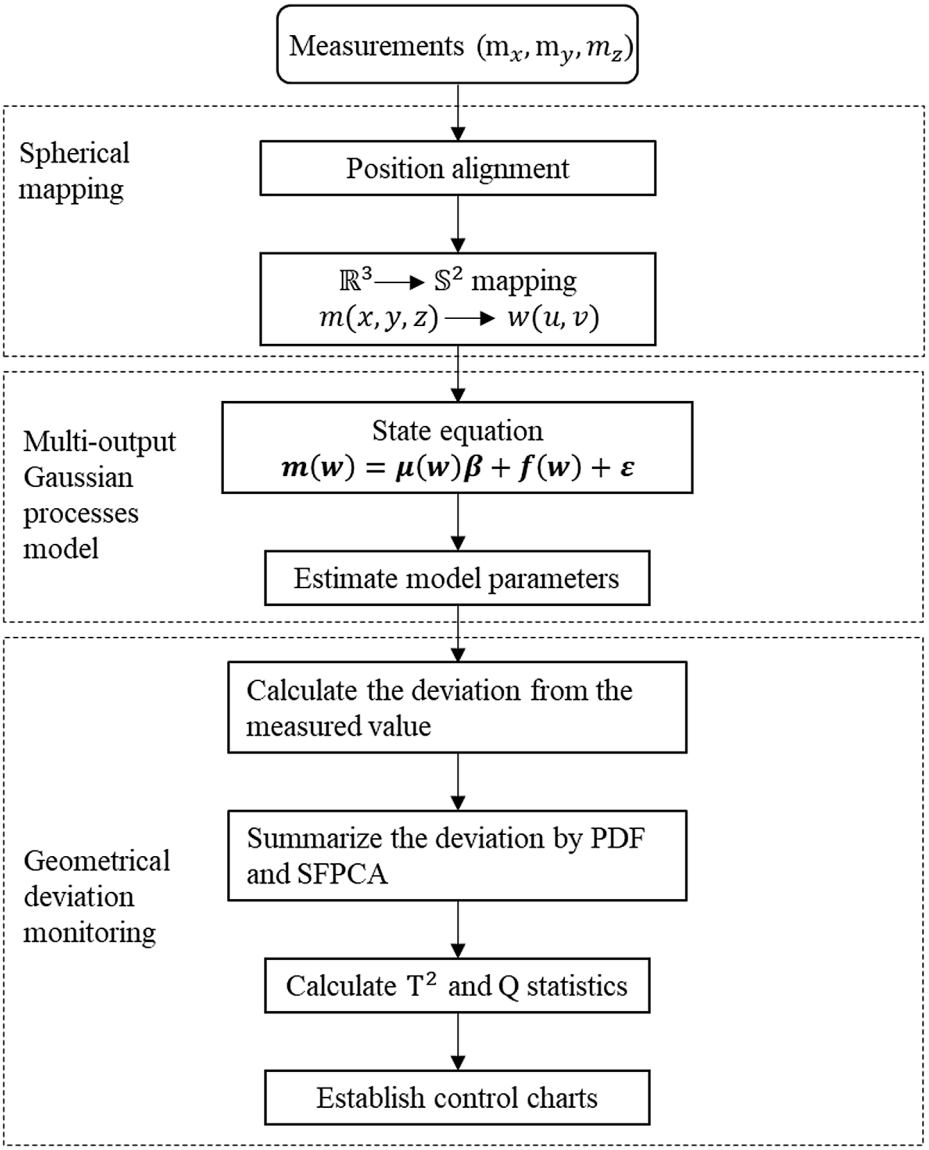

Fig. 3. Flowchart of the proposed method.

3. The proposed method

3.1. Model description

In this paper, the S-MOGP method based on spherical mapping and MOGP is proposed to model the 3D surface. In the proposed method, firstly, the 3D surface is parameterized through spherical mapping. Secondly, the surface shape is modeled via MOGP. Lastly, the T^2 and Q statistics are calculated to monitor the geometrical deviation of the 3D Surface. The main steps of this method are shown diagrammatically in Fig. 3.

There are three steps in the proposed method:

Step 1: Spherical mapping. First, position alignment is performed for the coordinate (m_x, m_y, m_z) of the measuring points on the surface. Then, parameterize the surface via spherical mapping. The coordinate value can be represented by two parameters: elevation (u) and azimuth (v). The center of the fitted ball is taken as the origin.

Step 2: Fitting MOGP model. Assuming the parametric surface $S(u,v)$ on $\mathbb{R}^2$ obeys the Gaussian distribution, and output function is a multivariate GP. The joint distribution of the training observation value and the predicted target can be obtained via Bayesian formula. Based on MOGP, the 3D surface is modeled and the model parameters are estimated.

Step 3: Deviation monitoring. Calculate the distance from the measured value to get a set of deviation values, and then the probability density function (PDF) and simplicial functional principal component analysis (SFPCA) are used to summarize the deviation. The T^2 and Q control charts are established to monitor the geometrical deviation.

3.2. Multi-output Gaussian processes model

As for each measured coordinate in $m = (m_x, m_y, m_z) \subset \mathbb{R}^3$, a transformation $f : \mathbb{R}^3 \to \mathbb{S}^2$ is established after spherical mapping. Therefore, a surface embedded in 3D space can be described by two parameters (u,v). The distance between two points is not expressed by Euclid distance but by angle value.

Parameterize the measuring point (m_x, m_y, m_z) on the spherical surface. Each point is represented by two parameters:

$$\mathrm{m}(w) = \begin{cases} m_x = x(u,v) \\ m_y = y(u,v) \\ m_z = z(u,v) \end{cases}, \; w = (u,v) \subset \mathbb{S}^2 \tag{11}$$

Establish the surface parameter equation: the input set is $\boldsymbol{w} = \{u_i, v_i\}_{i=1}^n$, that is, the measurement point corresponds to the parameter value through spherical mapping; the output set is the measured value of three coordinates $m = \{m_{x_i}, m_{y_i}, m_{z_i}\}_{i=1}^n$, where n is the number of measuring points. The proposed model includes three terms: the mean (the fixed effect), deviation (the correlation effect), and noise (the random effect), given by

$$\boldsymbol{m}(\boldsymbol{w}) = \boldsymbol{\mu}(\boldsymbol{w})^{\mathrm{T}}\boldsymbol{\beta} + \boldsymbol{f}(\boldsymbol{w}) + \boldsymbol{\varepsilon} \tag{12}$$

where $\boldsymbol{\mu}(\boldsymbol{w}) = \mathrm{diag}(\mu_x(\boldsymbol{w}), \mu_y(\boldsymbol{w}), \mu_z(\boldsymbol{w}))$ is a block diagonal matrix with blocks of $\{\mu_x = \cos u \cos v, \mu_y = \cos u \sin v, \mu_z = \sin u\}$, $\boldsymbol{\beta} = [\beta_1, \beta_2, \beta_3]^{\mathrm{T}}$ is a coefficient vector, $\boldsymbol{f}(\boldsymbol{w})$ is a multivariate random field which assumed to follow MOGP, and $\boldsymbol{\varepsilon}$ follows a normal distribution $N(0, \sigma^2 \boldsymbol{I})$.

In order to solve this model, it is needed to discuss the covariance structure. On the one hand, not all kernel functions are valid on the sphere. A random process is stationary on the sphere if its covariance function depends solely on the spherical angle. Huang et al. [35] discussed the validity of covariance functions on the sphere under different models based on the spherical angle distance. On the other hand, large spatial data set face tremendous computational challenges. A compactly supported function is identically zero outside a finite range, which can form a sparse covariance matrix to facilitate the calculation of large-scale data.

Therefore, a non-separable covariance is constructed combining the spherical covariance function and compactly supported function.

For two points $w_1(u_1, v_1)$ and $w_2(u_2, v_2)$ on $\mathbb{S}^d$, their spatial lag distance is the spherical distance between w_1 and w_2 on the largest circle on $\mathbb{S}^d$; more precisely, in our model, $w = (u,v)$, i.e., $d = 2$, the distance is

$$\theta(w_1, w_2) = \arccos\{\sin u_1 \sin u_2 + \cos u_1 \cos u_2 \cos(v_1 - v_2)\} \tag{13}$$

Then consider a covariance model with a compactly supported structure and discuss its effectiveness on sphere. A non-separable covariance based on compact supported structure can be derived by convolution approach according to Du et al. [36] Theorem 3,

$$C_{ij}(x) = \begin{cases} \int_0^1 (u - \|x\|)_+^{\nu} g_{ij}(u) du, & \|x\| \le 1, \\ 0, & \|x\| > 1, x \in \mathbb{R}^d, \end{cases} \quad i,j = 1, \cdots, m \tag{14}$$

where $g(x)$ is taken as the indicator function of a compact set in $\mathbb{R}^d$, and the function $g_{ij}(x)$ is continuous on $[0,1]$.

When $d \ge 2$, Du et al. [36] give an m-variate elliptically contoured random field with direct and cross covariances in Theorem 4, and then Ma et al. [37] proved the validity of the covariance on spherical $\mathbb{S}^d$. In our model, $d = 2$, the direct and cross covariances can be deduced as

$$C_{ii}(\theta) = \begin{cases} 2\alpha_i^2 \arccos(\tau_i(\theta)) - 2\alpha_i^2 \tau_i(\theta)\left(1 - \tau_i^2(\theta)\right)^{\frac{1}{2}}, & \theta \le 2\alpha_i \\ 0, & \theta > 2\alpha_i \end{cases} \tag{15}$$

$$C_{ij}(\theta) = \begin{cases} \pi \min\left\{\alpha_i^2, \alpha_j^2\right\}, & \theta \le |\alpha_i - \alpha_j| \\ \alpha_i^2 \arccos(\tau_i(\theta)) - \alpha_i^2 \tau_i(\theta)\left(1 - \tau_i^2(\theta)\right)^{\frac{1}{2}} & \\ + \alpha_j^2 \arccos(\tau_j(\theta)) - \alpha_j^2 \tau_j(\theta)\left(1 - \tau_j^2(\theta)\right)^{\frac{1}{2}}, & |\alpha_i - \alpha_j| \langle \theta \le \alpha_i + \alpha_j \\ 0, & \theta > \alpha_i + \alpha_j \end{cases} \tag{16}$$

where $\tau_i(\theta) = (\alpha_i^2 - \alpha_j^2 + \theta^2)/(2\alpha_i\theta)$ and $\tau_j(\theta) = (\alpha_j^2 - \alpha_i^2 + \theta^2)/(2\alpha_j\theta)$, $i \ne j$, $i,j = 1,2,3$.

Considering $\lambda = \{\beta, \alpha, \sigma\}$ as the set of hyper-parameters in the proposed model, the log-likelihood function is.

$$L = -\frac{3n}{2}\log(2\pi) - \frac{1}{2}\log|C + \sigma^2 \mathbf{I}| - \frac{1}{2}(\boldsymbol{m} - \boldsymbol{\mu\beta})^{\mathrm{T}}\left(C + \sigma^2 \mathbf{I}\right)^{-1}(\boldsymbol{m} - \boldsymbol{\mu\beta}) \tag{17}$$

By solving the hyperparameters, the 3D surface can be modeled from the measurement points.

3.3. Surface monitoring

In non-contact measurement, the dense point cloud data is usually high-dimensional, which makes it difficult to use ordinary control charts directly. In this method, the 3D surface is monitored by the deviation between the measured surface and the predicted value calculated by the S-MOGP model. In order to compare this geometric difference, it is necessary to establish an appropriate summary of the deviation values. Sample statistics (mean and variance) can be expressed, but will lead to the loss of a lot of information. Menafoglio et al. [38] proposed the method of summarizing the probability density function (PDF) of deviation values, which can strike a balance between retaining information and simplifying the deviation. Following this approach, the deviation values of 3D surfaces are summarized based on the PDF and principal component analysis (PCA) methods, and are monitored by the T^2 and Q control charts.

The S-MOGP model is established according to a nominal sample. For the j th measurement sample ($j = 1, \cdots, M$), the deviation value of a

measurement sample is calculated by

$$d_{ij} = \left\| m_{ij} - \widehat{z}_{ij} \right\| \tag{18}$$

where $\widehat{z}_{ij}$ is the prediction value, m_i is the true coordinates,$i = 1, \ldots, N_j$, and N_j is the number of measurement points of the j th sample.

Referring to the method proposed by Scimone et al. [39], PDF can be estimated from the Bernstein polynomial estimator. The PDF $\widehat{f}_j$ estimator based on empirical cumulative distribution function (CDF) F_j is given by

$$\widehat{f}_j(x) = N_j \sum_{k=0}^{N_j-1} \left[\left(F_j\left(\frac{k+1}{N_j}\right) - F_j\left(\frac{k}{N_j}\right) \right) b_{k,N_j}(x) \right] \tag{19}$$

where N_j is the number points in the point cloud, b_{k,N_j} is the k th Bernstein polynomial, $b_{k,N_j}(x) = N_j k x^k (1-x)^{N_j-k}$, and x is the variable transformation on a compact domain [0, 1].

Then, the simplicial functional principal component analysis (SFPCA) is performed to obtain the eigenvalues-eigenfunction (λ_i, ζ_i) of the sample covariance operator, and its scores along with the i th principal component as

$$S_{ij} = \left\langle \widehat{f}_j - \widehat{f}, \zeta_i \right\rangle \tag{20}$$

where $\widehat{f} = \frac{1}{M}\sum_{j=1}^{M} \widehat{f}_j$ is the sample mean.

Select a number $K \in \{1, \ldots, N\}$ of principal components which explain 98% of the total variability of the dataset. Considering two different statistics: T^2 statistic to identify anomalies in the K retained components and Q statistic to identify the prediction error. The statistics are calculated by

$$T_j^2 = \sum_{i=1}^{K} \frac{(S_{ij})^2}{\lambda_i} \tag{21}$$

$$Q = \left\langle \widehat{f}_j^{*} - \widehat{f}_j, \widehat{f}_j^{*} - \widehat{f}_j \right\rangle \tag{22}$$

where $\widehat{f}_j^{*} = \sum_{i=1}^{K} z_{ij}\zeta_i$ is the reconstruction of the j th density curve which retaining the first K principal components.

Two multivariate control charts are performed to monitor the T^2 and Q statistics. The upper control limits of T^2 and Q statistics are

$$\mathrm{UCL}_\alpha\left(T^2\right) = \frac{(N-1)^2}{N} q_{\mathrm{Beta}\left(1-\alpha, \frac{K}{2}, (N-k-1)/2\right)} \tag{23}$$

where q_{Beta} denotes the quantile of the Beta distribution and α is the Type I error probability.

$$\mathrm{UCL}_\alpha(Q) = \theta_1 \left\{ 1 - \theta_2 h_0 \left(\frac{1-h_0}{\theta_1^2} \right) + \frac{\sqrt{z_\alpha \left(2\theta_2 h_0^2\right)}}{\theta_1} \right\}^{\frac{1}{h_0}} \tag{24}$$

where z_α is the $(1-\alpha)$ quantile of the standard normal distribution, $h_0 = 1 - \frac{(2\theta_1\theta_3)}{3\theta_2^2}$, $\theta_r = \sum_{j=K+1}^{\infty} \lambda_j^r, r = 1, 2, 3$.

With the above steps, the deviation between the measured sample and the nominal surface model can be monitored by the Hotelling T^2 and Q control charts.

4. Simulation

4.1. Simulation surface prediction

In this section, three simulation surfaces with different shapes are generated to evaluate the surface modeling performance of the proposed method. The points on each surface are divided into training points and test points. The parameter model of the 3D surface is established through the training points and then the surface is predicted at the test points. To evaluate the performance of the model, the deviation of the predicted value from the true value is calculated by the mean square error (MSE):

$$\mathrm{MSE} = \sqrt{\frac{\sum_{i=1}^{n} \left| \widehat{z}_i - m_i \right|^2}{n}} \tag{25}$$

where $\widehat{z}_i$ is the prediction value, m_i is the true coordinates, n is the number of prediction points, and $|\bullet|$ denotes Euclidean distance.

In the ordinary GP model, the x and y coordinates of the measurement point are regarded as the interpretation variables, and the z coordinate is regarded as the response variable. Castillo et al. [25] replaced the Euclidean distance in the GP kernel function with the geodesic distance to model 3D surfaces, which can more accurately represent the correlation between the two points. In the simulation of surface prediction, the ordinary GP method, Geodesic Gaussian Processes (GGP) method [25] and GPLVM method [26] are used for method comparison. Three different surface forms including a sphere with four holes, a deformed cylinder, and a sinusoidal surface, shown in Fig. 4, are simulated for comparison.

1. Sphere with holes. A sphere with a radius of $R = 1$ and four holes is simulated to explore the modeling ability of the method on the surface with holes.
2. Deformed cylinder. A cylinder defined by a profile function: $2 + \alpha \times \cos(u)$ is simulated to explore the modeling ability of the method on the semi-closed surface, where α is the form factor and $\alpha = 1$ in the normal condition.
3. Sinusoidal surface. A sinusoidal surface defined by a profile function: $\beta \times \sin(u)$ is simulated to explore the modeling ability of the method on the non-closed and deployable surface, where β is the form factor and $\beta = 1$ in the normal condition.

For each simulation surface, error term with a mean value is 0 and variance is $\sigma^2(\sigma^2 = 0.01, 0.05, 0.1)$ in x, y, and z directions. Simulate 50 times for each situation and calculate the mean of MSE. In each situation, 400 points on the surface are generated, where 300 points are randomly selected as fitting points and the remaining 100 points are selected as prediction points. Table 1 shows the performance of a series of simulations of the four methods.

As shown in Table 1, for sphere with holes and deformed cylinder surfaces, the proposed method has the best prediction value. These two surfaces can be regarded as the deformation of an ordinary sphere. Therefore, compared with other methods, the proposed method can reflect the correlation between two points more exactly and can get the best prediction results. For the sinusoidal surface, the effect of S-MOGP is not as good as GGP and GPLVM methods. Because the GGP and GPLVM methods expand the sinusoidal surface into a plane, for deployable surfaces, planar mapping has less distortion. For sinusoidal surface, the spherical mapping method has great distortion. However, the proposed method is still better than the ordinary GP model.

According to the simulation results of three different types of surfaces, the proposed method has great advantages on closed and semi-closed surfaces, and the method is less affected by the noise. When the noise is large, it can still be closer to the true surface.

4.2. Simulation surface monitoring

The same surface model is used in the exact way as in the subsection 4.1 to monitor the geometrical deviations of surfaces. The control result is evaluated by the Average Run Length (ARL) value. The smaller the ARL value, the more sensitive the control chart is to abnormal changes and the better the method. To further assess the performance of the proposed method, the Q-Q plot method is used for comparison.

A Q-Q plot can test if two sets of data come from the same distribution. It plots the expected value of the specified distribution for each quantile in the sample data. If the resulting graph is linear, the sample

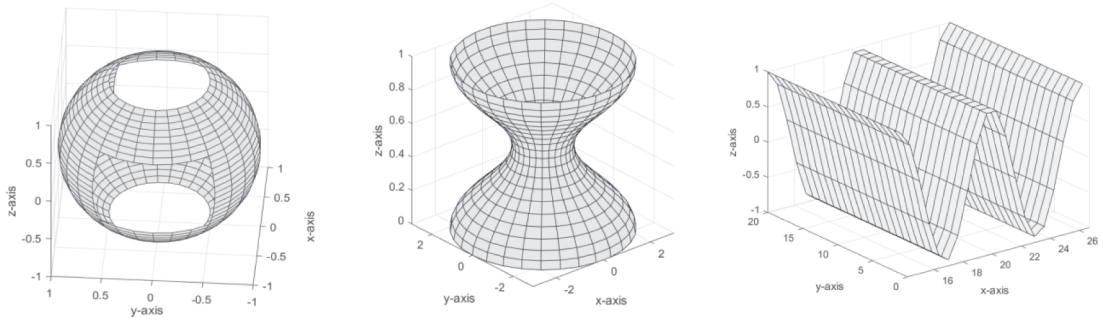

(a) Sphere with holes (b) Deformed cylinder (c) Sinusoidal surface

Fig. 4. Three simulated surfaces.

Table 1
Prediction results for three simulation surfaces.

shape	σ^2	MSE (S-MOGP)	MSE (GP)	MSE (GGP)	MSE (GPLVM)
Sphere with holes	0.01	0.0130	0.6732	0.4417	0.5466
	0.05	0.0438	0.7035	0.6733	0.6670
	0.1	0.0803	0.7321	0.7485	0.7044
Deformed cylinder	0.01	0.0241	0.5997	0.5443	0.4284
	0.05	0.0677	0.7479	0.7229	0.6400
	0.1	0.1032	0.7825	0.7383	0.7296
Sinusoidal surface	0.01	0.0332	0.1224	0.0089	0.0274
	0.05	0.0741	0.1932	0.0312	0.0707
	0.1	0.1439	0.2130	0.0674	0.1365

data is from the specified distribution. Wells et al. [19] compared the monitoring parameters of the Q-Q plot, including the intercept, slope, and two types of residual values. They concluded that in most cases, monitoring intercept and slope can provide the best monitoring results. Therefore, in this simulation, the intercept and slope of the Q-Q plot is monitored for method comparison.

To monitor the shape changes and noise changes of the simulated surface, for each simulation surface, simulating 500 samples for the normal process (phase I) to calculate the controlling parameters and the UCL. Assume type I error $\alpha = 0.005$. In Phase II, simulate the abnormal process 100 times (500 samples for each time) and calculate the mean and standard deviation of ARL under each method.

For the three simulation surfaces, assuming the form factor $R = 1$, $\alpha = 1$, $\beta = 1$ and noise factor $\sigma^2 = 0.01$ are the normal conditions, the proposed method and the Q-Q plot method are performed to compare the ARLs in Phase II. The simulation results are shown in Fig. 5.

Fig. 5 shows the ARLs of the proposed method and Q-Q plot method under different conditions. The proposed method has a better monitoring result than the Q-Q plot. This monitoring method can analyze the profile shape of the deviations, and the effect is better than the monitoring of the slope and intercept of the Q-Q plot.

This method can effectively and comprehensively reflect the information of the 3D surface. Compared with the Q-Q plot method, this method has a better monitoring effect and can identify abnormal information in the process more quickly.

5. Case study

The combustion chamber of the engine cylinder head is a complex 3D surface. If the surface of the combustion chamber has defects, it will affect the volume of the combustion chamber, which in turn affects the performance of the engine. Therefore, the research on the surface quality of the combustion chamber is very important.

The traditional method is based on the three-coordinate

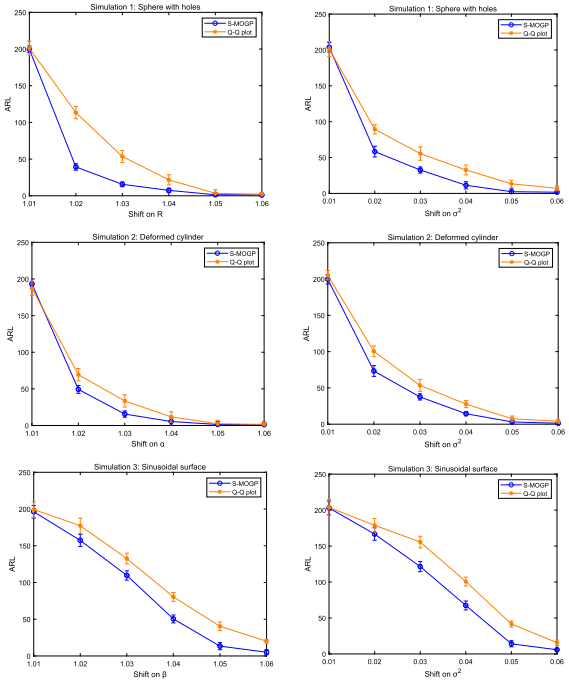

Fig. 5. ARLs and 95% confidence intervals in simulated surfaces 1, 2, 3 for S-MOGP and Q-Q plot methods.

measurement. The measurement area and number of points are selected artificially. It is difficult to express the overall contour of the combustion chamber surface. Due to the long measurement time, the interval measurement is used in this method, which is easy to miss the deviation in the batch.

The advanced HDM technology has fast measurement speed and the high-density point cloud data obtained by HDM can reflect the entire contour of the surface. Fig. 6 shows the measurement process of the HDM on the combustion chamber of the cylinder head. The cylinder head combustion chamber is scanned by line laser. Fig. 7 shows the measured point cloud data. In this experiment, the cylinder heads of eight B12 series engines in an automobile processing plant are measured. There are four combustion chambers on each cylinder head and a total of 32 combustion chambers are measured. Among them, due to mold wear, the cylinder head of the last engine was deformed. The proposed method is used to model and monitor these chambers.

The measurement results show that the combustion chamber is an approximately hemispherical structure with holes. Perform spherical mapping for each chamber point cloud, represented by (u, v).

First, explore the influence of the number of fitting points on the

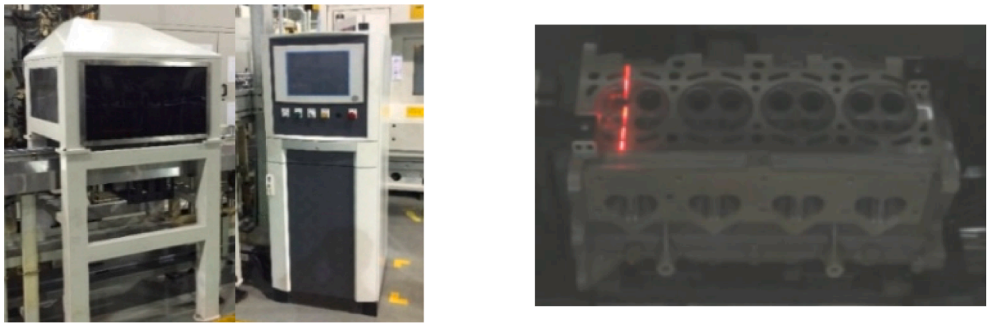

(a) HDM equipment (b) Line laser measurement process

Fig. 6. The measurement process of a cylinder head.

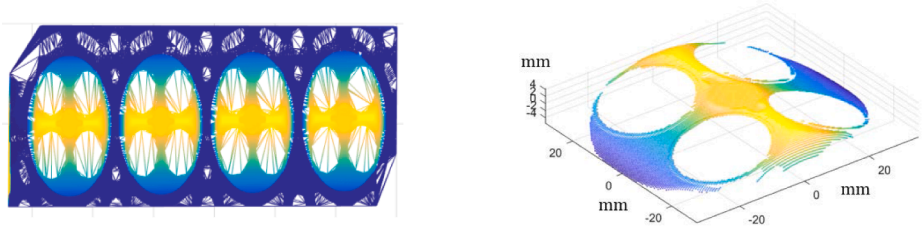

(a) Point cloud data of an engine cylinder head (b) Point cloud data of a chamber

Fig. 7. Measured point cloud data.

quality of the model. The original dataset consists of 9094 points from a combustion chamber (see Fig. 7(b)). Randomly select 500, 1500, 3500, 8000 points as fitting points (n_{fit}), and choose 1000 points as prediction points.

In the proposed method, the covariance with compactly supported structure can support the calculation of large-scale data. For the compared method GGP, Castillo et al. [25] used sparse matrix techniques to handle the inverse and determinant operations. The same method is applied to GPLVM model to compare the fitting effect of the model under large-scale measurement points.

Table 2 shows the MSE values of the three methods with different numbers of fitting points.

Comparing the proposed method S-MOGP with GP, GGP and GPLVM methods, the proposed method has the best prediction results. Moreover, for the surface with holes, the geodesic distance calculated by GGP has a large deformation from the true value, and the prediction result is not as good as the standard Euclidean GP model. The effect of the GPLVM model is between the GP and GGP. For this case, the spatial correlations are better modeled by spherical space rather than in geodesic space and Euclidean space.

Then monitoring the inner surfaces of the 32 combustion chambers. Among them, the 29th-32th cylinder head combustion chambers are defective products due to wear.

Taking the first 16 combustion chambers as phase I, and then the T^2 and Q control charts are established to monitor the next 16 combustion chambers, as shown in Fig. 8. The last four cavity surfaces have geometric deviations due to wear, which can be identified by the proposed method.

Last, the Q-Q plot is implemented for comparison. In the Q-Q plot method, each measured combustion chamber is compared with the first qualified sample to generate a Q-Q plot. The slope and intercept of the Q-Q plot are monitored by the Shewhart control chart. Fig. 9 shows the control chart of the Q-Q plot method. Fig. 9(a) shows the slope value of the Q-Q plot. A slope value closer to 1 indicates a smaller deviation between the sample and the qualified sample, so the slope control chart only indicates the lower control limit. Fig. 9(b) shows the intercept value of the Q-Q plot. The red lines are control limits. In this case, the last 4 samples are unqualified samples but only one unqualified sample is identified.

The experimental results show that compared with the GP, GGP and GPLVM method, the proposed method has the best fitting effect in this case, and can effectively model the inner surface of the engine cylinder head chamber. In this case, although the inner surface of the chamber is a non-closed surface, it is approximately hemispherical, and its spherical mapping has less distortion, so it is suitable to the proposed method. In the monitoring, the proposed method can effectively identify surface changes, which can quickly adjust the processing process to ensure product quality. The effectiveness of the method in practical application is verified by the fitting error and the monitoring process.

Table 2
The MSE of three methods.

n_{fit}	MSE(S-MOGP)	MSE(GP)	MSE(GGP)	MSE(GPLVM)
500	0.1007	0.3820	0.5168	0.3977
1500	0.0632	0.1284	0.3570	0.1446
3500	0.0619	0.1445	0.3696	0.1218
8000	0.0501	0.1109	0.3143	0.1169

6. Conclusions

This paper proposes an S-MOGP method based on spherical mapping and MOGP to model and monitor 3D surfaces. This method converts 3D coordinate values into spherical parameters through spherical mapping, establishes a state equation based on MOGP, and provides a control chart to monitor the geometrical deviations. The spherical distance is used to replace the Euclidean distance and geodesic distance. The effectiveness of this method for 3D surface modeling and monitoring is verified through simulations and an actual case.

Compared with the GP, GGP and GPLVM methods, the proposed

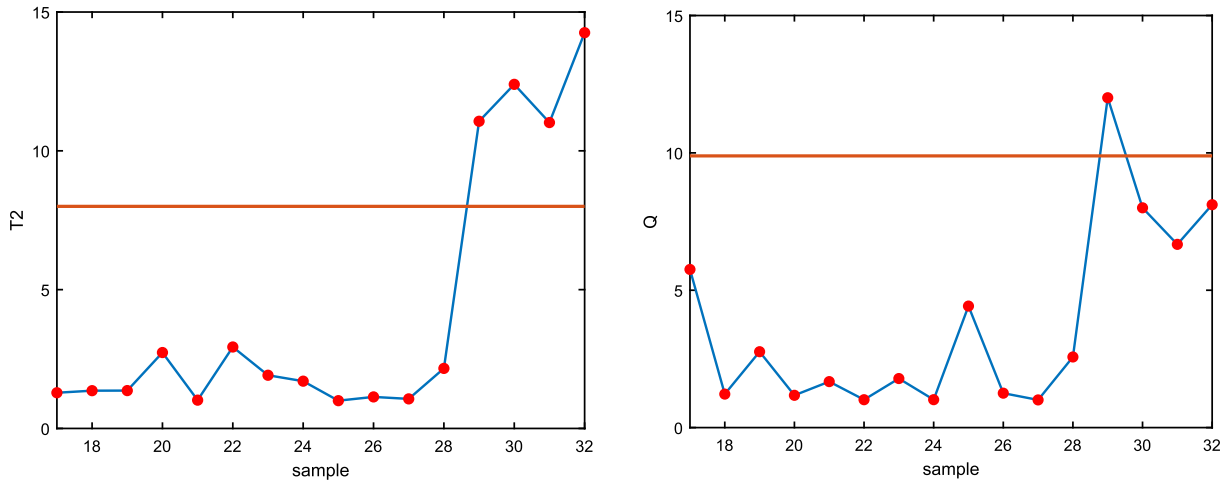

(a) T^2 control chart (b) Q control chart

Fig. 8. The control chart of S-MOGP.

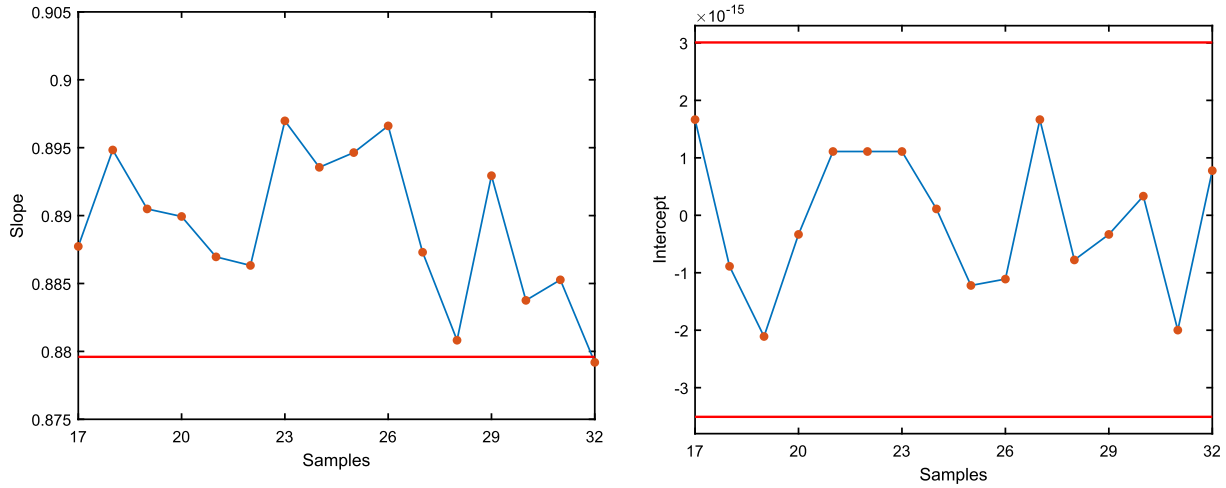

(a) Slope value of Q-Q plot (b) Intercept value of Q-Q plot

Fig. 9. The control chart of Q-Q plot.

method has the smallest prediction error on closed and semi-closed surfaces. In the actual case, the prediction accuracy of the proposed method is significantly increased. The proposed method comprehensively considers the spatial correlation in the three directions of x, y, and z. For spherical and multi-hole surfaces, the proposed method is not affected by the spatial distance between two points but only depends on the angle value, which can better model the 3D surface.

In surface monitoring, the proposed method can quickly identify abnormal conditions in the process. Compared with the Q-Q plot method, the proposed method can effectively identify surface changes and provide feedback information for the part processing process to ensure product quality.

In conclusion, this paper proposes an S-MOGP method for modeling and monitoring 3D surfaces. Compared with the existing methods, the proposed method has significant advantages on non-developable surfaces, especially on closed and multi-hole surfaces. Combined with the HDM technology, this method can be used in the processing of point cloud data on 3D surfaces. There are several possible directions for future research.

(1) At present, only offline data is used for analysis. This method can be combined with online HDM rapid measurement to realize real-time monitoring of 3D surfaces and reflect the online processing information.
(2) This method can monitor the change of surface shape, but it cannot identify the specific defect location. By combining image data and other processing methods, this method can be further explored to identify the location of surface defects.

CRediT authorship contribution statement

Chen Zhao: Methodology, Software, Writing – original draft. **Jun Lv:** Software, Data curation. **Shichang Du:** Writing – review & editing, Funding acquisition.

Declaration of Competing Interest

The authors declare that they have no known competing financial interests or personal relationships that could have appeared to influence the work reported in this paper.

Acknowledgments

The authors greatly acknowledge the editor and the reviewers for their valuable comments and suggestions that have led to a substantial improvement of the paper. This research was funded by major scientific and technological research and the project of "taking the lead" of Zhejiang Province, Ningbo City (Grant No. 2021Z093), Changshu leading talent plan for scientific and technological innovation and Entrepreneurship (Grant No.CSRC2066), and Gusu leading talent plan for scientific and technological innovation and Entrepreneurship (Grant No. ZXL2021021).

Appendix A

The specific process of spherical mapping.

1. Approximate the Laplace-Beltrami (LB) operator Δ on point cloud $P = \{z_1, z_2, \cdots, z_n\}$. Consider the approximation on the patch $N(z_s)$ of a point $z_s \in P$. For any function u defined on the neighborhood $N(z)$, it can be approximated by a combination of a set of basic function $\{f_s^1, f_s^2, \cdots, f_s^m\}$:

$$u = f_s(x, y) \approx \sum_{i=1}^{m} \widehat{c}_i f_s^i(x, y) \tag{a1}$$

Let $m = 6$, $\{1, x, y, x^2, xy, y^2\}$ are the basis of the space of all polynomials with second order or below. The coefficients $\widehat{c}_i$ can be approximated by the least square method. Since the LB operator is a second order differential operator, the LB operator of u is given by

$$\Delta u(z_s) = \alpha_1 \frac{\partial u}{\partial x}(z_s) + \alpha_2 \frac{\partial u}{\partial y}(z_s) + \alpha_3 \frac{\partial^2 u}{\partial x^2}(z_s) + \alpha_4 \frac{\partial^2 u}{\partial x \partial y}(z_s) + \alpha_5 \frac{\partial^2 u}{\partial y^2}(z_s) \tag{a2}$$

where α_i, $i = 1, \cdots, 5$, are coefficients which depend on partial derivatives of f_s.

2. Spherical conformal parameterization. Let Δ_{PC} represent the approximate LB operator on the point cloud. A conformal map $\phi : P \to \mathbb{C}$ is established if

$$\Delta_{PC}\phi = 0 \tag{a3}$$

where $\phi(a_i) = b_i$ for $i = 1, 2, 3$, and $a_i, b_i \in \mathbb{C}$. The a_1, a_2, a_3 are the three boundary points that are the regularity of a triangle of z_s.
The formula (4) is solved by boundary constraints. The spherical point cloud can be obtained by inverse stereographic projection P_N^{-1} on.$\phi(P)$

3. Correct the conformality distortion. First perform South Pole stereographic projection P_S, the spherical point cloud is projected back to the complex plane. The boundary constraints are updated with the outermost low-distortion data and are used to solve the Laplace equation $\psi : (P_S \circ P_N^{-1} \circ \phi)(P) \to \mathbb{C}$ by

$$\Delta_{PC}\psi = 0 \tag{a4}$$

Also, inverse stereographic projection P_S^{-1} is applied to obtain a composition map

$$\widetilde{f} = P_S^{-1} \circ \psi \circ P_S \circ P_N^{-1} \circ \phi \tag{a5}$$

According to (4) and (5), a conformal map $\widetilde{f} : P \to \mathbb{S}^2$ can be obtained.

4. Enhance parametric results through iteration. In each reiteration, perform the north-pole stereographic projection P_N, the spherical data is projected onto the complex plane and a harmonic map $\widetilde{\phi} : (P_N \circ \widetilde{f})(P) \to \mathbb{C}$ is solved by

$$\Delta_{PC}\widetilde{\phi} = 0 \tag{a6}$$

After obtaining $\widetilde{\phi}$, the inverse north-pole stereographic projection is employed again, and then the south-pole stereographic projection is employed. The corresponding harmonic map $\widetilde{\psi} : (P_S \circ P_N^{-1} \circ \widetilde{\phi} \circ P_N \circ \widetilde{f})(P) \to \mathbb{C}$ is solved by

$$\Delta_{PC}\widetilde{\psi} = 0 \tag{a7}$$

The new spherical parameterization is

$$P_S^{-1} \circ \widetilde{\psi} \circ P_S \circ P_N^{-1} \circ \widetilde{\phi} \circ P_N \circ \widetilde{f} \tag{a8}$$

Compare the updated parameterization result with the previous parameterization result $\widetilde{f}$. If unstable, repeat the process. The scheme algorithm is

Algorithm: Spherical mapping algorithm

Input: Point cloud P.
Output: Spherical mapping parameterization f.
1. Estimate the LB operator Δ_{PC} on P;
2. Solve the Laplace equation (3) by boundary constraints and obtain a conformal map $\phi : P \to \overline{\mathbb{C}}$;
3. Perform the inverse stereographic projection $P_N^{-1} : \overline{\mathbb{C}} \to \mathbb{S}^2$ on $\phi(P)$;
4. Perform the south-pole stereographic projection $P_S : \mathbb{S}^2 \to \overline{\mathbb{C}}$ on $(P_N^{-1} \circ \phi)(P)$;

(*continued on next page*)

(*continued*)

Algorithm: Spherical mapping algorithm

5. Correct the conformality distortion $\psi : (P_S \circ P_N^{-1} \circ \phi)(P) \to \mathbb{C}$;
6. Perform the inverse south-pole stereographic projection P_S^{-1} and obtain a composition map $f = P_S^{-1} \circ \psi \circ P_S \circ P_N^{-1} \circ \phi$;
7. **Repeat**
8. Update $\widetilde{f}$ by f;
9. Perform the north-pole stereographic projection $\widetilde{\phi} : (P_N \circ \widetilde{f})(P) \to \mathbb{C}$;
10. Perform the south-pole stereographic projection $\widetilde{\psi} : (P_S \circ P_N^{-1} \circ \widetilde{\phi} \circ P_N \circ \widetilde{f})(P) \to \mathbb{C}$;
11. Update f by $P_S^{-1} \circ \widetilde{\psi} \circ P_S \circ P_N^{-1} \circ \widetilde{\phi} \circ P_N \circ \widetilde{f}$;
12. **until** $mean(\|f(p_i) - \widetilde{f}(p_i)\|^2) < \epsilon$;

References

[1] X. Zhang, X. Wang, D. Wang, X. Wang, Z. Yao, L. Xi, Methodology to improve the cylindricity of engine cylinder bore by Honing, J. Manuf. Sci. E-T ASME 139 (3) (2017) 031008-031008-10, doi: 10.1115/MSEC2016-8709.

[2] Y. Shao, S. Du, H. Tang, An extended bi-dimensional empirical wavelet transform based filtering approach for engineering surface separation using high definition metrology, Measurement 178 (2021), 109259, https://doi.org/10.1016/j.measurement.2021.109259.

[3] G. Rajamohan, M.S. Shunmugam, G.L. Samuel, Effect of probe size and measurement strategies on assessment of freeform profile deviations using coordinate measuring machine, Measurement 44 (5) (2011) 832–841, https://doi.org/10.1016/j.measurement.2011.01.020.

[4] W.H. Woodall, Current research on profile monitoring, Production 17 (3) (2007) 420–425, https://doi.org/10.1590/S0103-65132007000300002.

[5] R.B. Kazemzadeh, R. Noorossana, A. Amiri, Phase I monitoring of polynomial profiles, Commun. 37 (10) (2008) 1671–1686, https://doi.org/10.1080/03610920. 701691714.

[6] C. Zou, F. Tsung, Z. Wang, Monitoring general linear profiles using multivariate exponentially weighted moving average schemes, Technometrics 49 (4) (2007) 395–408, https://doi.org/10.1198/004017007000000164.

[7] B.M. Colosimo, Q. Semeraro, M. Pacella, Statistical process control for geometric specifications: on the monitoring of roundness profiles, J. Qual. Technol. 40 (1) (2008) 1–18, https://doi.org/10.1080/00224065.2008.11917709.

[8] C. Zhao, S. Du, Y. Deng, G. Li, D. Huang, Circular and cylindrical profile monitoring considering spatial correlations, J. Manuf. Syst. 54 (2020) 35–49, https://doi.org/10.1016/j.jmsy.2019.11.011.

[9] L.J. Wells, R. Dastoorian, J.A. Camelio, A. Kusiak, A novel nurbs surface approach to statistically monitor manufacturing processes with point cloud data, J. Intell. Manuf. 32 (2) (2020) 329–345, https://doi.org/10.1007/s10845-020-01574-1.

[10] A. Wang, K. Wang, F. Tsung, Statistical surface monitoring by spatial-structure modeling, J. Qual. Technol. 46 (2014) 359–376, https://doi.org/10.1080/00224065. 2014.11917977.

[11] H. Lin, F. Keller, M. Stein, Influence and compensation of cmm geometric errors on 3d gear measurements, Measurement 151 (2) (2019), 107110, https://doi.org/10.1016/j.measurement.2019.107110.

[12] Y. Zang, P. Qiu, Phase I monitoring of spatial surface data from 3D printing, Technometrics 60 (2) (2018) 169–180, https://doi.org/10.1080/00401706.2017.1321585.

[13] Y. Zang, P. Qiu, Phase II monitoring of free-form surfaces: an application to 3D printing, J. Qual. Technol. 50 (4) (2018) 379–390, https://doi.org/10.1080/00224065.2018.1508274.

[14] S.E. Stankus, K.K. Castillo-Villar, An Improved multivariate generalised likelihood ratio control chart for the monitoring of point clouds from 3D laser scanners, Int. J. Prod. Res. 57 (8) (2019) 2344–2355, https://doi.org/10.1080/00207.543.2018.1518600.

[15] V. Mehrad, D. Xue, P. Gu, Prediction of surface reconstruction uncertainties for freeform surface inspection, Measurement 46 (8) (2013) 2682–2694, https://doi.org/10.1016/j.measurement.2013.04.025.

[16] H. Hagen, S. Hahmann, T. Schreiber, Visualization and computation of curvature behaviour of freeform curves and surfaces, Comput. Aided Des. 27 (7) (1995) 545–552, https://doi.org/10.1016/0010-4485(95)93587-P.

[17] K. Kase, A. Makinouchi, T. Nakagawa, H. Suzuki, F. Kimura, Shape error evaluation method of free-form surfaces, Comput. Aided Des. 31 (8) (1999) 495–505, https://doi.org/10.1016/S0010-4485(99)00046-9.

[18] K. Wang, F. Tsung, Using profile monitoring techniques for a data-rich environment with huge sample size, Qual. Reliab. Eng. Int. 21 (7) (2005) 677–688, https://doi.org/10.1002/qre.711.

[19] L.J. Wells, F.M. Megahed, C.B. Niziolek, J.A. Camelio, W.H. Woodall, Statistical process monitoring approach for high-density point clouds, J. Intell. Manuf. 24 (6) (2013) 1267–1279, https://doi.org/10.1007/s10845-012-0665-2.

[20] R. Osada, T. Funkhouser, B. Chazelle, D. Dobkin, Shape distributions, ACM Trans. Graph. 21 (4) (2002) 807–832, https://doi.org/10.1145/571647.571648.

[21] H. Laga, Y. Guo, H. Tabia, R.B. Fisher, M. Bennamoun, 3D Shape Analysis: Fundamentals, Theory and Application, John Wiley & Sons, Inc. 2019, doi: 10.3726/978-3-653-05106-3/4.

[22] D. Huang, S. Du, G. Li, C. Zhao, Y. Deng, Detection and monitoring of defects on three-dimensional curved surfaces based on high-density point cloud data, Precis. Eng. 53 (2018) 79–95, https://doi.org/10.1016/j.precisioneng.2018.03.001.

[23] B.M. Colosimo, P. Cicorella, M. Pacella, M. Blaco, From profile to surface monitoring: SPC for cylindrical surfaces via Gaussian Processes, J. Qual. Technol. 46 (2) (2014), https://doi.org/10.1080/00224065.2014.11917956.

[24] C. Zhao, J. Lv, S. Du, Y. Deng, Geometric error modeling and monitoring of the 3D surface by Gaussian Correlation Model, in: 2019 IEEE International Conference on Industrial Engineering and Engineering Management (IEEM), pp. 1022–1025, doi: 10.1109/IEEM44572.2019.8978691.

[25] E. Castillo, B.M. Colosimo, S.D. Tajbakhsh, Geodesic Gaussian processes for the parametric reconstruction of a free-form surface, Technometrics 57 (1) (2015) 87–99, https://doi.org/10.1080/00401706.2013.879075.

[26] N.D. Lawrence, Probabilistic non-linear principal component analysis with Gaussian process latent variable models, J. Mach. Learn. Res. 6 (3) (2005) 1783–1816, https://doi.org/10.1007/s10846-005-9019-z.

[27] C.E. Rasmussen, C.K.I. Williams, Gaussian Processes for Machine Learning, The MIT Press, 2006.

[28] X. Sun, P.L. Rosin, R.R. Martin, F.C. Langbein, Noise analysis and synthesis for 3D laser depth scanners, Graph. Models 71 (2) (2009) 34–48, https://doi.org/10.1016/j.gmod.2008.12.002.

[29] L. Shen, F. Makedon, Spherical mapping for processing of 3d closed surfaces, Image Vis. Comput. 24 (7) (2006) 743–761, https://doi.org/10.1016/j.imavis.2006.01.011.

[30] H. Liu, J. Cai, Y.S. Ong, Remarks on multi-output Gaussian process regression, Knowl. Based Syst. 144 (15) (2017) 102–121, https://doi.org/10.1016/j.knosys.2017.12.034.

[31] E. Praun, H. Hoppe, Spherical parametrization and remeshing, ACM Trans. Graph. 22 (3) (2003) 340–349, https://doi.org/10.1145/882262.882274.

[32] C. Brechbühler, G. Gerig, O. Kübler, Parametrization of closed surfaces for 3-d shape description, Comput. Vis. Image Und. 61 (2) (1995) 154–170, https://doi.org/10.1006/cviu.1995.1013.

[33] Z. Yao, Q. Zhao, X. Li, Q. Bi, Point cloud registration algorithm based on curvature feature similarity, Measurement 177 (11) (2021), 109274, https://doi.org/10.1016/j.measurement.2021.109274.

[34] P.T. Choi, K.T. Ho, L.M. Lui, Spherical conformal parameterization of genus-0 point clouds for meshing, SIAM J. Imaging Sci. 9 (4) (2015) 1582–1618, https://doi.org/10.1137/15M1037561.

[35] C. Huang, H. Zhang, S.M. Robeson, On the validity of commonly used covariance and variogram functions on the sphere, Math. Geosci. 43 (6) (2011) 721–733, https://doi.org/10.1007/s11004-011-9344-7.

[36] J. Du, C. Ma, Vector random fields with compactly supported covariance matrix functions, J. Stat. Plan. Infer 143 (3) (2013) 457–467, doi: 10.1016/j.jspi.2012.08.016.

[37] C. Ma, Stochastic representations of isotropic vector random fields on spheres, Stoch. Anal. Appl. 34 (3) (2016) 389–403, https://doi.org/10.1080/07362994.2015. 1136562.

[38] A. Menafoglio, M. Grasso, P. Secchi, B.M. Colosimo, Profile monitoring of probability density functions via simplicial functional PCA with application to image data, Technometrics 60 (4) (2018) 497–510, https://doi.org/10.1080/.00401706.2018.1437473.

[39] R. Scimone, T. Taormina, B.M. Colosimo, M. Grasso, P. Secchi, Statistical modeling and monitoring of geometrical deviations in complex shapes with application to Additive Manufacturing, Technometrics (2021) 1–34, https://doi.org/10.1080/00401706.2021.1961870.